oblateness-only fit at better than the 99% confidence level. Lydon and Sofia[9] also attempted to measure this shape term in 1992 and 1994 and obtained -0.40 ± 0.44 milliarcsec—consistent with zero, and significantly different from the $l = 4$ term we derive. Although the SOHO data yield the first evidence for a non-zero solar hexadecapole moment, the earlier measurements suggest that the Sun's high-order shape may change in time.

The 1996 data give consistent but noisier results, $c_2 = -6.00 \pm 0.80$ milliarcsec (in 1996, c_4 was indeterminate). The weighted average of our 1996 and 1997 data yield $c_2 = -5.38 \pm 0.39$ milliarcsec (the apparent solar radius was 972″). Figure 2 summarizes the status of many of the oblateness observations from the past 35 years. In contrast to the $l = 4$ shape measurements, the new MDI data, combined with the most recent results from refs 9 and 10, rule out any 11-year variability in c_2 larger than about 0.5 milliarcsec.

Figure 3 shows that the limb surface brightness, $B(\theta)$, varies with solar latitude. We express this fluctuation in terms of a photometric colour temperature variation by scaling $B(\theta)$ by $T_\odot/4$ (taking $T_\odot = 5{,}700$ K for the effective colour temperature). The Princeton–Michigan State–Caltech oblateness/limb photometer had the required accuracy to measure comparably small limb temperature changes, but averaged in relatively larger diametrically opposed limb regions. That experiment[3] also found a minimum in the solar limb temperature near ±55 degrees latitude. The MDI brightness profile obtained here is consistent with those earlier results.

The existence of a surface brightness variation (like the polar brightning in Fig. 3) that is not directly associated with photospheric magnetic fields is characteristic of most global models of the solar differential rotation. However, these data show that both the solar shape and brightness are more complicated than a simple quadrupole. It remains to be seen, in detail, what the implications are for our understanding of stellar convection, differential rotation and the solar cycle. If the tiny brightness variations we now see at the surface do 'shadow' the deep convection zone boundary (compare with ref. 2), then we can expect to detect a change in this temperature structure as the solar cycle evolves. Future MDI/SOHO observations should be able to confirm or refute this view. □

Received 22 September; accepted 8 December 1997.

1. Durney, B. R. & Roxburgh, I. Homogeneous convection and the equatorial acceleration. *Sol. Phys.* **16,** 2–20 (1971).
2. Kuhn, J. R. *The Structure of the Sun: VI. Winter School at IAC* (eds Roca Cortes, T. & Sanchez, F.) (Cambridge Univ. Press, 1996).
3. Kuhn, J. R., Libbrecht, K. G. & Dicke, R. H. The surface temperature of the Sun and changes in the solar constant. *Science* **242,** 908–911 (1988).
4. Schur, W. & Ambronn, L. Messungen des Sonnendurchmessers. *Astron. Mit. Koniglichen Stern. Zu Göttingen* 1–126 (1905).
5. Dicke, R. H. & Goldenberg, H. M. Solar oblateness and general relativity. *Phys. Rev. Lett.* **18,** 313–316 (1967).
6. Hill, H. A. & Stebbins, R. T. The intrinsic visual oblateness of the Sun. *Astrophys. J.* **200,** 471–483 (1987).
7. Dicke, R. H., Kuhn, J. R. & Libbrecht, K. G. Is the solar oblateness variable? *Astrophys. J.* **318,** 471–483 (1975).
8. Beardsley, B. *The Visual Shape and Multipole Moments of the Sun.* Thesis, Univ. Arizona (1987).
9. Rösch, J., Rozelot, J. P., Deslandes, H. & Desnoux, V. A new estimate of the quadrupole moment of the Sun. *Solar Phys.* **165,** 1–11 (1996).
10. Lydon, T. J. & Sofia, S. A measurement of the shape of the solar disk. *Phys. Rev. Lett.* **76,** 177–179 (1996).
11. Rozelot, J. P. & Rösch, J. An upper bound to the solar oblateness. *Solar Phys.* **172,** 11–18 (1997).
12. Scherrer, P. H. *et al. The Solar Oscillations Investigation—Michelson Doppler Imager: The SOHO Mission* (eds Fleck, B., Domingo, V. & Polland, A.) (Kluwer, Holland, 1995).
13. Kuhn, J. R. *et al. Sounding Solar and Stellar Interiors* (ed. Berthomieu, G.) (Kluwer, Holland, 1997).
14. Lites, B. The extreme limb of the Sun. *Sol. Phys.* **85,** 193–210 (1983).
15. Kuhn, J. R., Lin, H. & Loranz, D. Gain calibrating nonuniform image-array data using only the image data. *Publ. Astron. Soc. Pacif.* **103,** 1097–1108 (1991).

Acknowledgements. We thank J. Saba, C. DeForest and J. Covington for their assistance in operating the MDI instrument; L. Allen, H. Schweitzer, J.-P. Olive and K. Miller for the planning and execution of SOHO roll manoeuvres; and the SOHO flight operations team, including H. Benefield, N. Piston and B. Sapper, for making these activities run flawlessly. This work was supported by NASA. We dedicate this work to the memory of Robert H. Dicke, who inspired a generation of astrophysicists to consider the measurement and interpretation of the shape of the Sun.

Correspondence and requests for materials should be addressed to J.R.K. (e-mail address: jkuhn@solar.stanford.edu).

Destruction of the Fermi surface in underdoped high-T_c superconductors

M. R. Norman*, H. Ding*†, M. Randeria‡, J. C. Campuzano*†, T. Yokoya§, T. Takeuchi‖, T. Takahashi§, T. Mochiku¶, K. Kadowaki#, P. Guptasarma* & D. G. Hinks*

* *Materials Science Division, Argonne National Laboratory, Argonne, Illinois 60439, USA*
† *Department of Physics, University of Illinois at Chicago, Chicago, Illinois 60607, USA*
‡ *Tata Institute of Fundamental Research, Mumbai 400005, India*
§ *Department of Physics, Tohoku University, 980 Sendai, Japan*
‖ *Department of Crystalline Materials Science,Nagoya University, Nagoya 464-01, Japan*
¶ *National Research Institute for Metals, Sengen, Tsukuba, Ibaraki 305, Japan*
# *Institute of Materials Science, University of Tsukuba, Ibaraki 305, Japan*

The Fermi surface—the set of points in momentum space describing gapless electronic excitations—is a central concept in the theory of metals. In this context, the normal 'metallic' state of the optimally doped high-temperature superconductors is not very unusual: above the superconducting transition temperature, T_c, there is evidence for a large Fermi surface[1–3] despite the absence of well-defined elementary excitations. In contrast, the normal state of underdoped high-temperature superconductors differs in that there is evidence for a 'pseudogap' above T_c (refs 4–6). Here we examine, using angle-resolved photoemission spectroscopy, the temperature dependence of the Fermi surface in underdoped $Bi_2Sr_2CaCu_2O_{8+\delta}$. We find that, on cooling the sample, the pseudogap opens up at different temperatures for different points in momentum space. This leads to an initial breakup of the Fermi surface, at a temperature T^*, into disconnected arcs, which then shrink with decreasing temperature before collapsing to the point nodes of the superconducting ground state below T_c. This unusual behaviour, where the Fermi surface does not form a continuous contour in momentum space as in conventional metals, is unprecedented in that it occurs in the absence of long-range order. Moreover, although the superconducting gap below T_c evolves smoothly into the pseudogap above T_c, the pseudogap differs in its unusual temperature-dependent anisotropy, implying an intimate but non-trivial relationship between the pseudogap and the superconducting gap.

Angle-resolved photoemission spectroscopy (ARPES) probes the occupied part of the electron spectrum, and for quasi-two-dimensional systems its intensity $I(\mathbf{k}, \omega)$ as a function of momentum $\mathbf{k}$ and frequency ω is proportional to the Fermi function $f(\omega)$ times the one-electron spectral function $A(\mathbf{k}, \omega)$ (ref. 3). In Fig. 1a–c, the solid curves are ARPES spectra for an underdoped '85 K' sample of $Bi_2Sr_2CaCu_2O_{8+\delta}$ (Bi2212) at three $\mathbf{k}$ points a, b and c, respectively, on the Fermi surface (determined above T^*) for various temperatures. (Here the Bi2212 samples are distinguished by their onset T_c, in this case, 85 K.) We look first at the superconducting state data at $T = 14$ K. At each $\mathbf{k}$ point, the sample spectra are pushed back to positive binding energy ($\omega < 0$) due to the superconducting gap, and we also see a resolution-limited peak associated with a well-defined quasiparticle excitation in the superconducting state. The superconducting gap, as estimated by the position of the midpoint of the leading edge of the spectrum, is seen to decrease as one moves from point 'a' near $\bar{M}$ to 'b' to 'c', closer to the diagonal $\Gamma - Y$ direction (notation is described in Fig. 1 legend), consistent with a $d_{x^2-y^2}$ order parameter. Next, we consider the changes in Fig. 1 as a function of increasing T. At each $\mathbf{k}$ point the quasiparticle

peak disappears above T_c, but the suppression of spectral weight—the pseudogap—persists well above T_c, as noted in earlier work[4–6].

The striking new feature which is apparent from Fig. 1 is that the pseudogap at different **k** points closes at different temperatures, with larger gaps persisting to higher *T*s. At point a, near $\bar{M}$, there is a pseudogap at all *T*s below 180 K, at which the Bi2212 leading edge matches that of Pt. We take this as the definition of T^* (ref. 5) above which the largest pseudogap has vanished within the resolution of our experiment, and a closed contour of gapless excitations—a Fermi surface—is obtained[7]. The surprise is that if we move along this Fermi surface to point b the sample leading edge matches Pt at 120 K, which is smaller than T^*. Continuing to point c, about halfway to the diagonal direction, we find that the Bi2212 and Pt leading edges match at an even lower temperature of 95 K. In addition, we have measured spectra on the same sample along the Fermi contour near the ΓY line and found no gap at any *T*, even below T_c, consistent with $d_{x^2-y^2}$ anisotropy.

One simple way to quantify the behaviour of the gap is to plot the midpoint of the leading edge of the spectrum (Fig. 1e). We will say that the pseudogap has closed at a **k** point when the midpoint equals zero energy, in accordance with the discussion above. From this plot, we find that the pseudogap closes at point a at a *T* above 180 K, at point b at 120 K, and at point c just below 95 K. If we now view these data as a function of decreasing *T*, the picture of Fig. 2 clearly emerges. The pseudogap suppression first opens up near $(\pi, 0)$ and progressively removes larger portions of the Fermi contour, leading to gapless arcs which shrink with decreasing *T*. We note that midpoints with negative binding energy, particularly for **k** point c, indicate the formation of a peak in the spectral function at $\omega = 0$ as *T* increases.

We see similar results on other underdoped samples of Bi2212. For example, in the upper panel of Fig. 3 we show midpoints for a 77 K underdoped sample at two **k** points shown in the inset, with behaviour very similar to that of the 85 K sample of Fig. 1. This behaviour may be compared with that of the more conventional *T*-dependence of an overdoped 87 K sample as shown in the lower panel. Gaps with different magnitudes, one at a **k** point near $\bar{M}$ and the other halfway towards the ΓY direction, go to zero at the same temperature, very close to T_c; we have also seen this in other overdoped samples. This is in marked contrast with the new results on underdoped samples. Further, to show that the negative midpoints at high *T*s are not unusual, we plot those for an 82 K overdoped sample at the $\bar{M}$Y Fermi point as filled symbols in the lower panel of Fig. 3. The midpoint goes to zero at about T_c

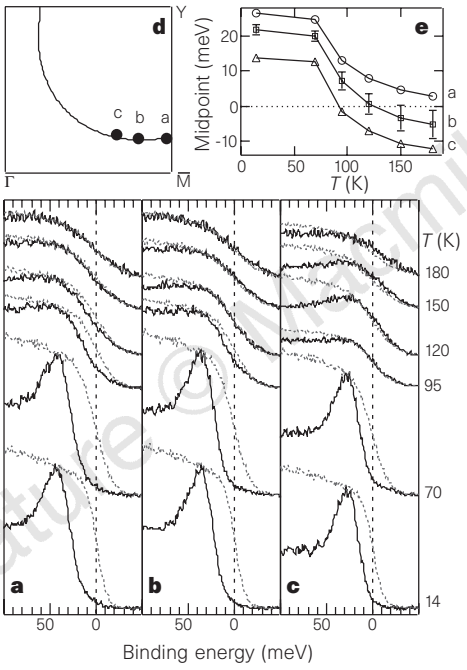

Figure 1 Data obtained on single crystals of Bi2212 grown by the travelling solvent floating-zone method. Doping was achieved by adjusting the oxygen partial pressure during annealing with samples labelled by their onset T_cs. Measurements were carried out at the Synchrotron Radiation Center, Wisconsin, using a high resolution 4-m normal incidence monochromator with 22-eV photons and an energy resolution of 20 meV (full-width at half-maximum). The spectra in **a–c** are taken at three **k** points in the Brillouin zone, shown in **d**, for an 85 K underdoped Bi2212 sample at various temperatures (solid curves). (The Y quadrant was studied to minimize effects due to the superlattice[12].) Our notation is $\Gamma = (0, 0)$, $\bar{M} = (\pi, 0)$ and $Y = (\pi, \pi)$, in units of $1/a$, where a is the Cu–Cu distance, and ΓM̄ is along the CuO bond direction. The dotted curves are reference spectra from polycrystalline Pt (in electrical contact with the sample) used to determine the chemical potential (zero binding energy). Note the closing of the spectral gap at different *T* for different **k**. This feature is also apparent in the plot (**e**) of the midpoint of the leading edge of the spectra as a function of *T*.

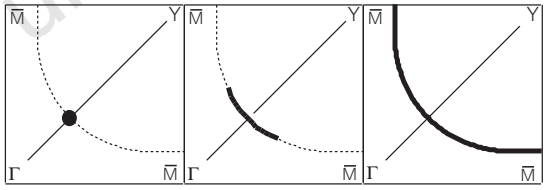

Figure 2 Schematic illustration of the temperature evolution of the Fermi surface in underdoped copper oxides. The *d*-wave node below T_c (left panel) becomes a gapless arc above T_c (middle panel) which expands with increasing *T* to form the full Fermi surface at T^* (right panel).

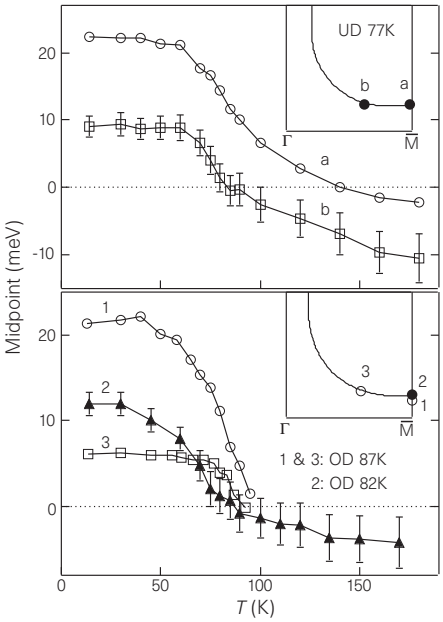

Figure 3 Midpoints of the leading edge of the ARPES spectra of Bi2212 samples, plotted against temperature. Top panel, data for a 77 K underdoped (UD) sample, again showing closure of the spectral gap at different *T* for different **k**. This behaviour can be contrasted with that of overdoped samples (bottom panel) where all gaps close near T_c.

(indicating the absence of a pseudogap above T_c in this sample) followed by a slower evolution to negative binding energy (indicating the formation of a spectral peak, as discussed above). There are also important differences between the spectral lineshapes of the overdoped and underdoped cases. The underdoped spectra are broader above T_c, as demonstrated by the flatness of the spectra seen in Fig. 1 at **k** points a and b, and have smaller quasiparticle peaks below T_c, implying an increase in the strength of the interactions as the doping is reduced.

Before discussing the implications of our results, we introduce a visualization aid that makes these results easier to understand. This symmetrization method, described in Fig. 4 legend, effectively eliminates the Fermi function f from ARPES data and permits us to focus directly on the spectral function A. We have extensively checked this method, and have studied in detail the errors introduced by incorrect determination of either the chemical potential or the Fermi momentum $\mathbf{k}_F$ (which lead to spurious narrow features in the symmetrized spectra); we have also studied the effect of the small (1° radius) **k**-window of the experiment (this effect was found to be small).

In Fig. 4a–c we show symmetrized spectra for the 85 K underdoped sample corresponding to the raw data of Fig. 1a–c, respectively. To emphasize that the symmetry is put in by hand, we show the $\omega > 0$ curve as a dotted line. In Fig. 4a at **k** point a near $\bar{M}$, the sharp quasiparticle peak disappears above T_c but a strong pseudogap suppression, on the same scale as the superconducting gap, persists all the way up to 180 K (T^*). In Fig. 4b and c we again see pseudogap depressions on the scale of the superconducting gaps at those points, but the pseudogap fills up at lower temperatures: 120 K at b and 95 K at c. In Fig. 4c, moreover, a spectral peak at zero energy emerges as T is raised. All of the conclusions drawn from the raw data in Figs 1 and 3 are obvious from the simple symmetrization analysis of Fig. 4.

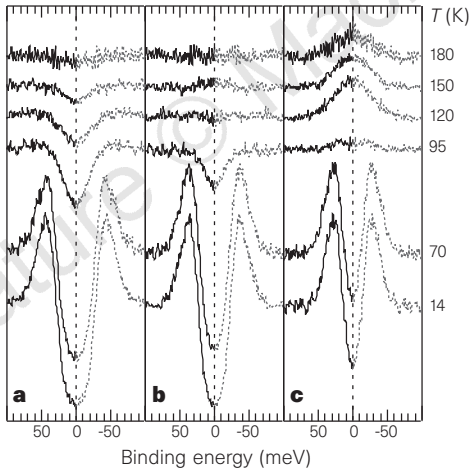

Figure 4 Results of symmetrization analyses. Given ARPES data described[3] by $I(\omega) = \Sigma_k I_0 f(\omega) A(\mathbf{k}, \omega)$ (with the sum over a small momentum window about the Fermi momentum $\mathbf{k}_F$), we can generate the symmetrized spectrum $I(\omega) + I(-\omega)$. Making the reasonable assumption of particle–hole (p–h) symmetry for a small range of ω and $\epsilon_{\mathbf{k}}$, we have $A(\epsilon_{\mathbf{k}}, \omega) = A(-\epsilon_{\mathbf{k}}, -\omega)$ for $|\omega|, |\epsilon_{\mathbf{k}}|$ less than few tens of meV (where $\epsilon_{\mathbf{k}}$ are the bare energies). It then follows, using the identity $f(-\omega) = 1 - f(\omega)$, that $I(\omega) + I(-\omega) = \Sigma_k I_0 A(\mathbf{k}, \omega)$ which is true even after convolution with a (symmetric) energy resolution function. This symmetrized spectrum coincides with the raw data for $\omega \leqslant -2.2T_{\text{eff}}$, where $4.4T_{\text{eff}}$ is the 10–90% width of the Pt leading edge, which includes the effects of both temperature and resolution. Non-trivial information is obtained for the range $|\omega| \leqslant 2.2T_{\text{eff}}$, which is then the scale on which p–h symmetry has to be valid. The curves are symmetrized spectra corresponding to the raw spectra of Fig. 1. The gap closing in the raw spectrum of Fig. 1 corresponds to where the pseudogap depression disappears in the symmetrized spectrum. We note the appearance of a spectral peak at higher temperatures in **c**.

We now discuss why the T dependence of the Fermi arc is not simply due to inelastic scattering above T_c broadening the d-wave node. From Fig. 4, it is apparent that the gap 'fills in' for **k** points a and b as T is raised, whereas it 'closes' for **k** point c as a peak at zero energy emerges. This can be seen more clearly in Fig. 5, where we show symmetrized spectra for a 75 K underdoped sample of Bi2212 at two **k** points (similar to points a and c of Fig. 4) as a function of temperature. For the first point (I; top panel), the spectral feature at the gap edge does not move with temperature, whereas for the latter point (II; bottom panel), it clearly moves in to zero energy.

A unique feature of ARPES is that it provides **k**-resolved information. We believe that the unusual T-dependence of the pseudogap anisotropy will be a very important factor in reconciling the different crossovers seen in the pseudogap regime by different probes, each of which measures a **k**-sum weighted with a different set of **k**-dependent matrix elements or kinematical factors (such as Fermi velocity). For instance, quantities which involve the Fermi velocity, such as the d.c. resistivity above T_c and the penetration depth below T_c (superfluid density), should be sensitive to the region near the ΓY direction, and would thus be affected by the behaviour we see at **k** point c. Other types of measurements (such as specific heat and tunnelling) are more 'zone-averaged' and will have significant contributions from **k** points a and b as well, so should see a more pronounced pseudogap effect. Other data that we have indicate that the region in the Brillouin zone where behaviour like **k**-point c is seen shrinks as the doping is reduced, and thus appears to be correlated with the loss of superfluid density[8]. Further, we speculate that the disconnected Fermi arcs should have a profound influence on magnetotransport, given the lack of a continuous Fermi contour in momentum space.

We emphasize that the Fermi arcs do not imply the existence of hole pockets (that is, small closed contours) centred about $(\pi/2, \pi/2)$, as suggested by some theories of lightly doped Mott insulators (for a review, see ref. 9). In the samples studied here (and more heavily underdoped ones) we have carefully searched for hole pockets and for shadow band dispersion, but found no evidence for either[7]. The

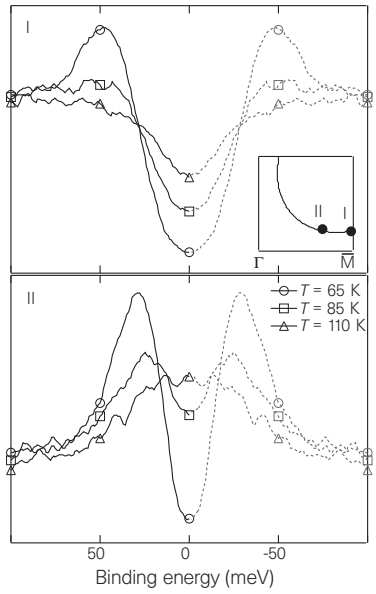

Figure 5 Symmetrized spectra for a 75 K underdoped sample of Bi2212, at three different temperatures. The **k** points are analogous to a and c of Fig. 4. We note that the spectral feature at the gap edge does not move in energy with increasing T for point I (top panel), but does move in to zero energy for point II (bottom panel).

gapless arcs that we observe are simply an intermediate state in the smooth evolution of *d*-wave nodes into a full Fermi surface. This smooth evolution was carefully checked on an 83 K underdoped sample where a detailed sweep was done in **k** space at $T = 90$ K, revealing only a small Fermi arc just above T_c. This behaviour is fully consistent with the gap above and below T_c being of the same origin as suggested by our earlier experiments[5,7].

Theoretical calculations in which *d*-wave pairing correlations cause a pseudogap above T_c (ref. 10) have predicted gapless arcs which expand as T increases. Resonating valence bond theories also lead to gapless arcs above T_c due to spinon pairing[11]. There are other proposals in which the pseudogap has a completely different (non-pairing) origin from the superconducting gap. Given the smooth evolution that we find through T_c, such proposals seem difficult to reconcile with our results. □

Received 23 July; accepted 22 December 1997.

1. Campuzano, J. C. *et al.* The Fermi surfaces of $YBa_2Cu_3O_{6.9}$ as seen by angle-resolved photoemission. *Phys. Rev. Lett.* **64,** 2308–2312 (1990).
2. Olson, C. G. *et al.* High-resolution angle-resolved photoemission study of the Fermi surface and normal-state electronic structure of $Bi_2Sr_2CaCu_2O_8$. *Phys. Rev. B* **42,** 381–386 (1990).
3. Randeria, M. *et al.* Momentum distribution sum rule for angle-resolved photoemission. *Phys. Rev. Lett.* **74,** 4951–4954 (1995).
4. Marshall, D. S. *et al.* Unconventional electronic structure evolution with hole doping in $Bi_2Sr_2CaCu_2O_{8+\delta}$: angle-resolved photoemission results. *Phys. Rev. Lett.* **76,** 4841–4844 (1996).
5. Ding, H. *et al.* Spectroscopic evidence for a pseudogap in the normal state of underdoped high-T_c superconductors. *Nature* **382,** 51–54 (1996).
6. Loeser, A. G. *et al.* Excitation gap in the normal state of underdoped $Bi_2Sr_2CaCu_2O_{8+\delta}$. *Science* **273,** 325–329 (1996).
7. Ding, H. *et al.* Evolution of the Fermi surface with carrier concentration in $Bi_2Sr_2CaCu_2O_{8+\delta}$. *Phys. Rev. Lett.* **78,** 2628–2631 (1997).
8. Uemura, Y. J. *et al.* Universal correlations between T_c and n_s/m^* in high-T_c cuprate superconductors. *Phys. Rev. Lett.* **62,** 2317–2320 (1989).
9. Lee, P. A. in *High Temperature Superconductivity* (eds Bedell, K. S. *et al.*) 96–116 (Addison-Wesley, New York, 1990).
10. Engelbrecht, J. R., Nazarenko, A., Randeria, M. & Dagotto, E. Pseudogap above T_c in a model with $d_{x^2-y^2}$ pairing. Preprint available at http://xxx.lanl.gov/archive/cond-mat/9705166
11. Wen, X. G. & Lee, P. A. Theory of underdoped cuprates. *Phys. Rev. Lett.* **76,** 503–506 (1996).
12. Ding, H. *et al.* Angle-resolved photoemission spectroscopy study of the superconducting gap anisotropy of $Bi_2Sr_2CaCu_2O_{8+x}$. *Phys. Rev. B* **54,** R9678–B9681 (1996).

Acknowledgements. We thank J. Sadleir and A. Kaminski for their help. This work was supported by the US Dept of Energy Basic Energy Sciences, the US NSF, the NSF Science and Technology Center for Superconductivity, the CREST of JST, and the Ministry of Education, Science and Culture of Japan. The Synchrotron Radiation Center is supported by the NSF.

Correspondence and requests for materials should be addressed to J.C.C. (e-mail: jcc@uic.edu).

A nanometre-scale mechanical electrometer

A. N. Cleland* & M. L. Roukes

Condensed Matter Physics 114-36, California Institute of Technology, Pasadena, California 91125, USA

The mechanical detection of charge has a long history, dating back more than 200 years to Coulomb's torsion-balance electrometer[1]. The modern analogues of such instruments are semiconductor-based field-effect devices, the most sensitive of which are cryogenically cooled single-electron transistors[2]. But although these latter devices have extremely high charge sensitivity, they suffer from limited bandwidth and must be operated at millikelvin temperatures in order to reduce thermal noise. Here we report the fabrication and characterization of a working nanometre-scale mechanical electrometer. We achieve a charge sensitivity of 0.1 e Hz$^{-0.5}$, competitive with conventional semiconductor field-effect transistors; moreover, thermal noise analysis indicates that the nanometre-scale electrometer should ultimately reach sensitivities of the order of 10^{-6} e Hz$^{-0.5}$, comparable with charge-detection capabilities of cryogenic single-electron transistors. The nanometre-scale electrometer has the additional advantages of high temperature (≥4.2 K) operation and response over a larger bandwidth, from which a diversity of applications may result.

We have described elsewhere[3] the techniques used to fabricate and measure devices of the type reported here. An electron micrograph and a schematic view of our nanomechanical electrometer is shown in Fig. 1. It consists of three principal components: electrodes, which experience an attractive force when a small charge is applied; a compliant mechanical element that moves in response to this force; and a displacement detector that provides a means of monitoring the motion. The mechanical element is a two-element torsional resonator with a spring constant G_0 and moment I. Its fundamental torsional resonance frequency is ω_0, and its mechanical loss is parametrized by a quality factor $Q = \omega_0/\Delta\omega$, where $\Delta\omega$ is the frequency width of the resonant response at half maximum.

The device includes three electrodes: two for inducing and measuring the mechanical response of the structure, and one for coupling charge, which alters this response. Two electrodes consist of metal loops tracing the boundaries of the outer and inner paddles, while the opposing metal gate electrode is fixed to the stationary substrate, at a distance d from the inner paddle. The mutual capacitance between the gate electrode and the inner paddle is represented by the parameter C. To measure a small charge, the gate electrode is biased by a charge q_0, which yields an electrostatic force $F_E = q_0^2/Cd$. Small changes in the coupled charge, δq, about the bias point q_0 alter the force by an amount $f_E = 2\delta q E_0$, where E_0 is the equilibrium electric field. This results in an effective torsional spring constant $G_{eff} = G_0 + g$, where $g = -r\partial q\partial E_0/\partial\theta$ (θ is the paddle torsion angle, E_θ the field component along the unit vector θ, and r the paddle's radial dimension). This gives rise to a shift away from the unperturbed resonance frequency, $\delta\omega/\omega_0 \approx g/2G_0$.

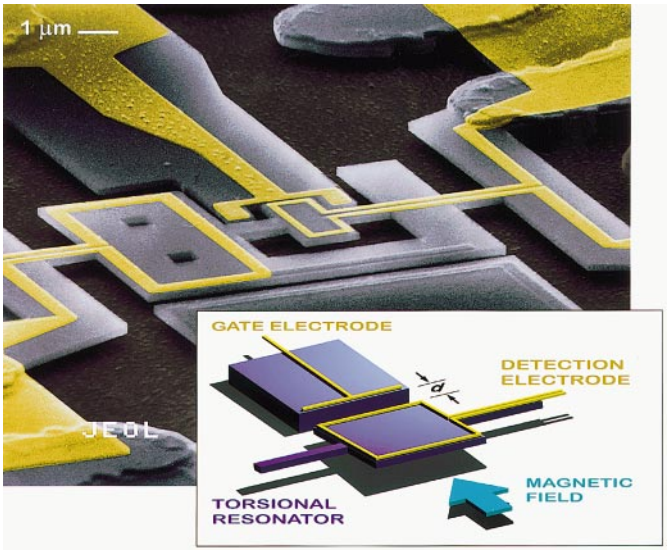

Figure 1 Nanometre-scale charge detector. The inset schematically depicts its principal components: torsional mechanical resonator, detection electrode, and gate electrode used to couple charge to the mechanical element. A external, parallel magnetic field is employed for readout. In the actual device (main figure) a double torsional element is used with moment I, torsional spring constant G_0 (calculated to be 1.1×10^{-10} N m), and spacing, $d = 0.5$ μm, between the gate and inner paddle electrodes. The fundamental resonance frequency of the structure is 2.61 MHz, with a quality factor measured to be $Q = 6{,}500$; the coupling capacitance between the gate and resonator was calculated to be $C = 0.4$ fF (H. Pothier, D. Esteve and M. H. Devoret, personal communication). The resonator was fabricated from a single-crystal Si-on-insulator substrate, with a 0.2-μm-thick Si layer on a 0.4-μm insulating layer. The Au electrodes and resonator structure are patterned using electron beam lithography. The smallest lateral feature in the structure is 0.2 μm, so there is scope to scale these devices to even smaller dimensions. This could ultimately yield bandwidths in the GHz regime.

* Present address: Department of Physics, UC Santa Barbara, Santa Barbara, California 93106, USA.